ORGANOMETALLICS
Article
pubs.acs.org/Organometallics

Photochemical Production of Ethane from an Iridium Methyl Complex

Catherine L. Pitman and Alexander J. M. Miller*

Department of Chemistry, University of North Carolina at Chapel Hill, Chapel Hill, North Carolina 27599-3290, United States

Supporting Information

ABSTRACT: An iridium methyl complex, $[Cp^*Ir(bpy)(CH_3)]^+$, was prepared by electrophilic methylation of Cp*Ir(bpy) with CH_3I and characterized electrochemically, photophysically, crystallographically, and computationally. Irradiation of the MLCT transition of $[Cp^*Ir(bpy)(CH_3)]^+$ in the presence of CH_3I in acetonitrile produces ethane, methane, propionitrile, and succinonitrile. A series of mechanistic studies indicates that C−C bond formation is mediated by free methyl radicals produced through monometallic photochemical homolysis of the Ir−CH_3 bond.

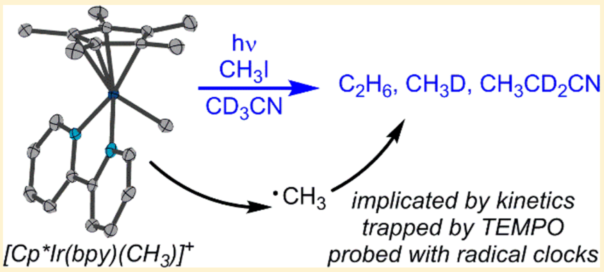

INTRODUCTION

Photocatalysts capable of mediating C−C bond formation could play an important role in the light-driven generation of energy-dense liquid fuels. Ethane formation from two methyl fragments is the simplest C−C bond forming reaction leading to an alkane, and organometallic methyl complexes have been the subject of photophysical and photochemical inquiry. Though photochemical ethane generation has been observed from metal methyl complexes,[1] such reactivity is notably uncommon.[2]

Many approaches to integrating light absorption with C−C bond formation have been explored. In photoredox catalysis, photosensitizers can trigger C−C bond formation following an excited state electron transfer.[3,4] Photochemical ligand dissociation (which opens a coordination site and triggers migratory insertion) and M−C bond homolysis (leading to radical reactivity) can also form C−C bonds.[5] Radicals are a common component of metal alkyl photochemistry. In the 1980s, Crabtree investigated Hg sensitization, which produces radicals, for various alkane functionalizations.[6] Platinum complexes are also known to couple two alkyl ligands on a single site through a radical mechanism.[7]

In thinking of ways to develop photochemical C−C bond formation, we drew inspiration from our recently discovered, bimolecular mechanism for H−H bond formation from a monohydride.[8] Quantum yields of hydrogen production nearing unity can be achieved when irradiating $[Cp^*Ir(bpy)(H)]^+$ ($[\mathbf{1}]^+$; Cp* is η^5-pentamethylcyclopentadienyl and bpy is 2,2′-bipyridine) in the presence of acids in CH_3CN. The bond formation is initiated by electron transfer between excited state $[\mathbf{1}]^{+*}$ and ground state $[\mathbf{1}]^+$, producing the reactive species $Cp^*Ir^{II}(bpy)(H)$ and $[Cp^*Ir^{IV}(bpy)(H)]^{2+}$ that together form H_2. This mechanism allows a slightly endergonic excited state electron transfer process to be coupled to an exergonic bond formation.

Given that the Cp*Ir(bpy) scaffold facilitates efficient bimetallic coupling for H_2 evolution, we questioned whether substitution of a methyl for the hydride could lead to C−C bond formation. Herein we report the synthesis and characterization of the methyl complex, $[Cp^*Ir(bpy)(CH_3)]^+$ ($[\mathbf{2}]^+$) and our mechanistic investigation of its photochemical C−C bond formation reactivity.

RESULTS AND DISCUSSION

Synthesis and Characterization of an Ir Methyl Complex. Previously unreported methyl complex $[Cp^*Ir(bpy)(CH_3)][I]$ ($[\mathbf{2}][I]$) was synthesized by electrophilic methylation of the Ir(I) precursor Cp*Ir(bpy) (**3**). A 50 mM solution of CH_3I in Et_2O was added dropwise to a purple solution of Cp*Ir(bpy) in Et_2O, resulting in precipitation of $[\mathbf{2}][I]$ as a fluffy yellow solid. The ^1H NMR spectrum in CD_3CN shows the expected four aromatic resonances of bpy, the 15H singlet of Cp*, and an upfield 3H singlet at δ −0.04. The ^{13}C NMR spectrum features a methyl resonance (δ −6.35).

Vapor diffusion of Et_2O into a solution of $[\mathbf{2}][I]$ in CH_3CN produced yellow crystals suitable for X-ray diffraction (XRD). Complex $[\mathbf{2}][I]$ takes on a "piano stool" structure with a methyl ligand and an outer sphere iodide ion (Figure 1). The Ir−CH_3 distance (2.147(5) Å) falls into the range of other reported Cp*Ir−CH_3 distances (2.03−2.22 Å; see Supporting Information for full details).[9] The Ir center, however, is not centered below the Cp* ring: The carbons *trans* to methyl form bonds to Ir (Ir−C13 2.235(5) Å and Ir−C14 2.236(4) Å) longer than those *cis* to methyl (Ir−C11 2.186(4) Å, Ir−C12 2.176(4) Å, Ir−C15 2.189(4) Å). The structure of $[Cp^*Ir(bpy)(Cl)][ClO_4]$, by contrast, features Ir−C distances that do not vary around the cyclopentadienyl ring (2.163 Å).[10] The

Received: March 6, 2017

DOI: 10.1021/acs.organomet.7b00175
Organometallics XXXX, XXX, XXX−XXX

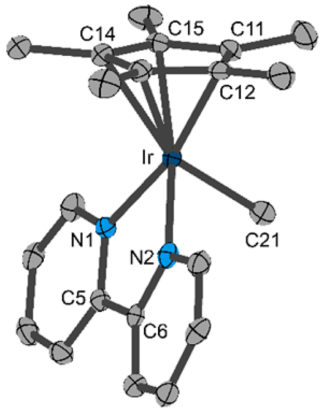

Figure 1. Structural representation of [**2**][I] with ellipsoids drawn at the 50% probability level. Hydrogen atoms and iodide counterion omitted for clarity. Selected distances (Å): Ir−C21 2.147(5), C5−C6 1.458(6).

structure of [**1**][PF_6][11] displays the same asymmetry found in the structure of [**2**][I], suggesting that this asymmetry is indicative of methyl and hydride ligands acting as strong σ-donors in [**2**][I] and [**1**][PF_6].

A structural comparison of Ir(III) complex [**2**]$^+$ with reduced Ir(I) precursor **3** was sought. A large purple block crystal suitable for XRD was produced by slow evaporation of a solution of **3** in THF. The report of this crystal structure completes the group 9 Cp*M(bpy) series (M = Co, Rh, and Ir).[12−14] Like the lighter metal congeners, **3** adopts a near-perpendicular orientation of the Cp* and bpy planes (84.68°, Figure 2). The C−C bond connecting the pyridine rings of bpy (C5−C6 1.403(5) Å) shows the characteristic contraction observed in these electron-rich species, attributed to electron delocalization into bpy resulting in partial double-bond character in the interpyridyl bond. In free bipyridine, this distance is 1.49 Å and contracts to 1.43 Å in bpy$^{\bullet-}$ and 1.39 Å for bpy^{2-}.[15] In Ir complex **3**, however, this bond is shorter than that in either of the lighter brethren (M = Co, 1.419 Å;[12] M = Rh, 1.423 Å),[13,14] suggesting that more electron density resides on bpy when M = Ir.

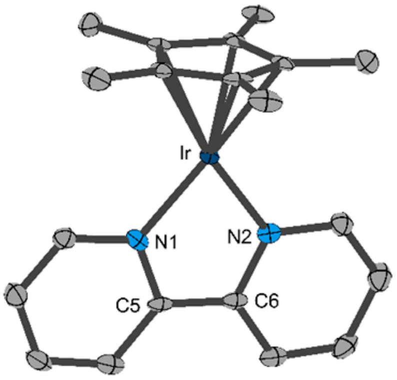

Figure 2. Structural representation of **3** with ellipsoids drawn at the 50% probability level. Hydrogen atoms omitted for clarity. Selected distance (Å): C5−C6 1.403(5).

The structure of [**2**][I] features a substantially longer C5−C6 distance (1.458(6) Å) than that found in **3**. The interpyridyl distance in [**2**][I] is similar to that of [Cp*Ir(bpy)(Cl)][ClO_4] (1.463(11) Å), in which the bpy is not considered to be partially reduced.

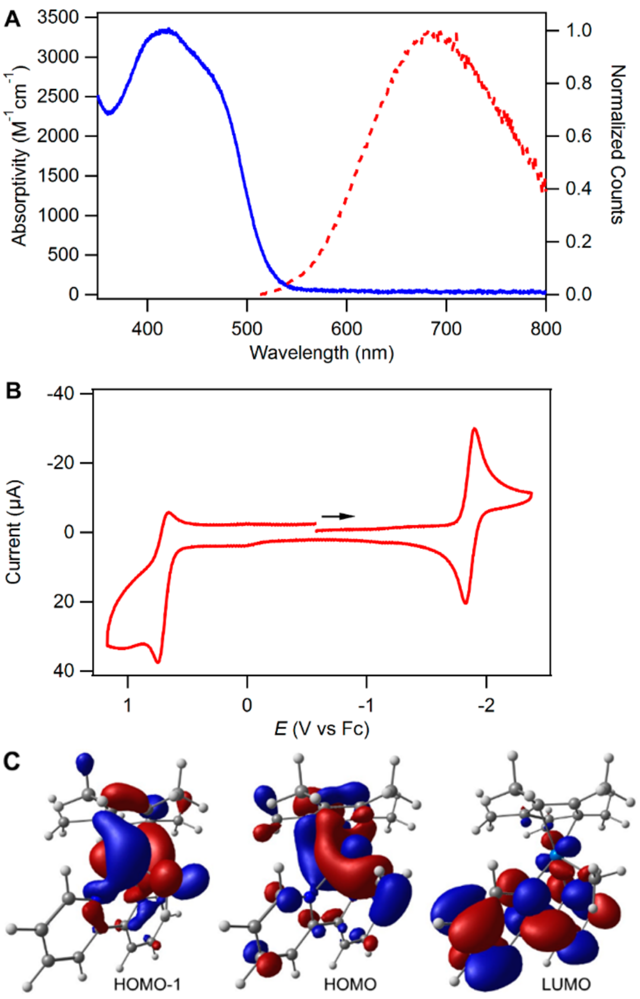

Figure 3. (A) Absorptivity (solid blue) and normalized emission (dashed red) of [**2**]$^+$ in CH_3CN solution. Excitation at 420 nm. (B) Cyclic voltammogram of 1 mM [**2**]$^+$ in CH_3CN with 0.1 M [$^nBu_4N$][PF_6] under an atmosphere of N_2. Scan rate 0.25 V·s^{-1}. (C) Orbitals from TD-DFT involved in the lowest energy transitions at 450 and 442 nm.

In acetonitrile, the UV−vis spectrum of [**2**]$^+$ shows an absorbance with λ_{max} = 418 nm (ε_{max} = 3300 M^{-1} cm^{-1}, Figure 3A). The absorbance of [**2**]$^+$ is best fit by two Gaussians centered at 413 and 476 nm that are estimated to have extinction coefficients of 3300 and 1100 M^{-1} cm^{-1}, respectively (Figure S9). To explore the nature of the orbitals involved in these transitions, we turned to time-dependent density functional theory (TD-DFT). The singlet ground-state structure of [**2**]$^+$ was optimized using the M06 functional (LANL2DZ ECP basis set for the Ir atom and 6-311G** for all other atoms), modeling acetonitrile solvation with a polarized continuum model. Absorption properties in acetonitrile were explored using TD-DFT from the optimized ground-state geometry (see Supporting Information for full details). The transitions at 450 nm (f = 0.0161) and 442 nm (f = 0.0937) reflect the observed spectrum: Both calculation and experiment feature two transitions under the MLCT with the weaker feature at a longer wavelength. According to TD-DFT, both transitions arise out of mixed HOMO and HOMO−1 states to

Table 1. Comparison of Electrochemical and Photophysical Features of [**1**]$^+$ and [**2**]$^+$

parameter	X = CH$_3$	X = H
$E°$(III/II)	−1.82 V	−1.80 V[8]
$E°$(IV/III)	0.74 V	0.50 V[8]
λ_{MLCT}, [Cp*Ir^{III}(bpy)(X)]$^+$	418 nm (3300 $M^{-1}cm^{-1}$)	428 nm (3000 M^{-1} cm^{-1})[18]
emission max, [Cp*Ir^{III}(bpy)(X)]$^+$	702 nm	708 nm[8]
ΔG_{ST}	50 kcal·mol^{-1}	47−52 kcal·mol^{-1}[18]
$E°$(III*/II)	0.35 V	0.37 V[8]
$E°$(IV/III*)	−1.42 V	−1.67 V[8]

the LUMO. The HOMO is a bonding interaction between a d-orbital of Ir and the methyl C-p$_z$ orbital (z-axis along the Ir-CH$_3$ vector). HOMO−1, however, is an antibonding interaction between Ir-d$_{xz}$ and methyl C-p$_x$ orbitals (Figure 3C). The LUMO is primarily bpy π*-based.

The absorbance spectrum of analogous Ir hydride [**1**]$^+$ in CH$_3$CN has a single Gaussian MLCT transition at 428 (3000 M^{-1} cm^{-1}), ascribed to a charge transfer from a σ bonding HOMO (with Ir d-orbital and hydride s-orbital character) to a bpy π* LUMO.[16] While the LUMOs of [**1**]$^+$ and [**2**]$^+$ are similar, the presence of p-orbitals in the methyl ligand account for the spectral differences.

Upon irradiation into the MLCT absorbance of [**2**][I] (excitation at 420 nm), no steady-state emission was observed at room temperature in CH$_3$CN. Hypothesizing that the iodide counteranion was quenching the excited state,[17] counterion exchange was carried out by addition of excess NH$_4$PF$_6$ to a 9:1 H$_2$O/MeOH solution of [**2**][I], resulting in precipitation of [Cp*Ir(bpy)(CH$_3$)][PF$_6$] ([**2**][PF$_6$]) as a light yellow powder.

Metathesized salt [**2**][PF$_6$] is weakly emissive at room temperature. In CH$_3$CN solution, excitation at 420 nm produces a broad emission feature at 702 nm with a photoluminescence quantum yield of 0.04% (Figure 3A). The excitation spectrum of [**2**][PF$_6$] aligns with the MLCT feature of the absorbance spectrum. The energy between the singlet ground state and the triplet excited state (ΔG_{ST}) can be estimated by extrapolation of the high-energy edge of the emission feature to the baseline, giving ΔG_{ST} = 50 kcal·mol^{-1} (Figure S11).

The electronic structure of methyl complex [**2**]$^+$ was investigated by cyclic voltammetry. A 1 mM solution of [**2**][PF$_6$] was prepared in CH$_3$CN containing 0.1 M [^{n}Bu$_4$N][PF$_6$]. A reversible reduction (ΔE_p = 77 mV, $i_{p,c}/i_{p,a}$ = 0.94) of [**2**]$^+$ was observed at $E_{1/2}$ = −1.82 V and a nearly irreversible oxidation (ΔE_p = 95 mV, $i_{p,a}/i_{p,c}$ = 0.30 at 0.25 V·s^{-1}) was observed at $E_{1/2}$ = 0.74 V (Figure 3B). The reduction, formally Ir(III) to Ir(II), may also be described as a bpy-based reduction, [**2**]$^+$/Cp*Ir^{III}(bpy$^{\bullet -}$)(CH$_3$). The oxidation, formally [**2**]$^+$/[Cp*Ir^{IV}(bpy)(CH$_3$)]$^{2+}$, extends across the Cp*, Ir, and CH$_3$ fragments according to our DFT. Excited state reduction potentials can be calculated from the ground state potentials and ΔG_{ST} (see Supporting Information for full details). The excited state can be reduced at $E°$(III*/II) = 0.35 V, and it can be oxidized at $E°$(IV/III*) = −1.42 V.

Our initial hypothesis was that methyl [**2**]$^+$ might undergo similar excited state reactivity to hydride [**1**]$^+$, which undergoes self-quenching electron transfer from an MLCT excited state. To determine the energetics of self-quenching of [**2**]$^+$, the driving force for electron transfer between excited state [**2**]$^{+*}$ and ground state [**2**]$^+$ ($\Delta G°_{ET}$) can be determined using either an excited state and ground state potential (0.74 V − 0.35 V = 0.39 V) or according to eq 1. $\Delta G°_{ET}$ is determined to be about 9 kcal·mol^{-1} endergonic. Though a sizable barrier, it may be surmountable when coupled to a thermodynamically favorable chemical step, as has been observed for uphill electron transfers with [Ru(bpy)$_3$]$^{2+}$.[19] Self-quenching of [**1**]$^+$ is ~3 kcal·mol^{-1} endergonic and occurs with high efficiency at high concentration.[8]

$$\Delta G°_{ET} = 23.06(E°(IV/III)) - 23.06(E°(III/II)) - \Delta G_{ST} \quad (1)$$

From the comparison of electrochemical and photophysical properties of hydride [**1**]$^+$ and methyl [**2**]$^+$ in Table 1 and from the structural features discussed above, the electronic similarities of the complexes are apparent. The similarity of the emission features of [**1**]$^+$ and [**2**]$^+$ gives rise to similar ΔG_{ST}; the value of ΔG_{ST} of 50 kcal·mol^{-1} determined here for [**2**]$^+$ falls within the range of 47 kcal·mol^{-1} < ΔG_{ST} < 52 kcal·mol^{-1} previously determined for [**1**]$^+$.[8] While the reduction potentials of [**1**]$^+$ and [**2**]$^+$ are similar, the oxidation of [**2**]$^+$ is 240 mV more positive than that of [**1**]$^+$. Additionally, this oxidation is noticeably more reversible for [**2**]$^+$ than that for [**1**]$^+$. Fast scan rates (200 V·s^{-1}) were required to observe the rereduction process for hydride [**1**]$^+$,[8] but for methyl [**2**]$^+$, a reduction feature is apparent even at a scan rate of 0.05 V·s^{-1} (Figure S13).

Photochemical Production of Ethane and Methane. Encouraged by the similarities in the electronic structures of [**1**]$^+$ and [**2**]$^+$, we sought to probe for similarities in photochemical reactivity. Inspired by the ability of [**1**]$^+$ to undergo light-induced H$_2$ formation in the presence of a H$^+$ source, we considered the analogous reaction for C−C bond formation: light-induced ethane formation from [**2**]$^+$ and a CH$_3$$^+$ source.

A CD$_3$CN solution of [**2**][PF$_6$], excess CH$_3$I, and a mesitylene internal standard was illuminated with a 443 nm LED for 3.5 h (Figure S14). ^{1}H NMR spectroscopic analysis showed the characteristic resonances of ethane, methane, and propionitrile. Product yields were determined by measuring gaseous concentrations by headspace GC and by measuring dissolved gases by ^{1}H NMR spectroscopy. Yields are reported relative to [**2**]$^+$ consumed in the reactions. Ethane, methane, and propionitrile were produced in 19, 39, and 9% yield, respectively. As hypothesized, photolysis of [**2**]$^+$ forms C−C bonds.

The primary Ir-containing species after photolysis was [Cp*Ir(bpy)(I)]$^+$ ([**4**]$^+$, 95%). Iodide [**4**]$^+$ was observed by HR-MS (ESI$^+$) in solutions after photolysis, and [**4**]$^+$ was also independently prepared by addition of 3 equiv of NaI to a solution of [Cp*Ir(bpy)(OH$_2$)][OTf]$_2$ in CD$_3$CN. The resulting ^{1}H NMR spectrum was consistent with that of the product of photolysis. The UV−vis spectrum of [**4**]$^+$ in CH$_3$CN shows an absorbance at λ_{max} = 375 nm (2500 M^{-1} cm^{-1}).

DOI: 10.1021/acs.organomet.7b00175

Weaker CH_3^+ sources were also investigated. Samples of [**2**][I] with CH_3OTs (OTs is tosylate) in CD_3CN were irradiated with 443 nm light for 22 h (Figure S15). Ethane and methane, but not propionitrile, were observed by ^1H NMR spectroscopy. The appearance of some of the same products suggests that the reaction may be proceeding through the same mechanism as with CH_3I.

Mechanistic Considerations. Scheme 1 shows several possible reaction pathways from the excited state of $[\mathbf{2}]^+$.

Scheme 1. Possible Reaction Pathways of Metal Methyls from the Excited State

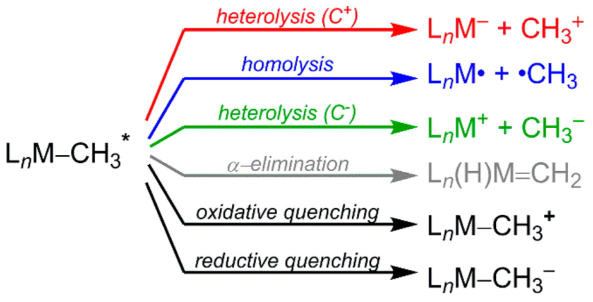

Reactions that lead to bond breaking are shown in color and electron transfers shown in black. Photochemical *α*-elimination is typically observed in early metal dimethyl species (gray)[20] and is thus considered unlikely in the present late metal monomethyl system. To probe for CH_3^+ formation, $[\mathbf{2}]^+$ was irradiated at 443 nm in CD_3CN with 7 equiv of pyridine to act as a CH_3^+ trap through the formation of 1-methylpyridinium. No reaction was observed over 5 h of photolysis. To ensure that the reaction was not reversed upon stopping photolysis, Ir(I) complex **3** and 5 equiv of 1,4-dimethylpyridinium iodide in CD_3CN were allowed to mix in the dark for 24 h. No methylation of **3** was observed; thus, the red pathway of Scheme 1 forming methyl cation is unlikely to be operative.

To investigate the other mechanistic possibilities, we examined the intermediates that would lead to ethane formation for two likely reactions: a self-quenching mechanism (Scheme 2, top) and a radical homolysis mechanism (Scheme 2, bottom). In the case of self-quenching, the methyl ligands of 2 equiv of $[\mathbf{2}]^+$ couple in order to make ethane. Further reaction of resultant **3** with CH_3I would regenerate $[\mathbf{2}]^+$. With a radical homolysis pathway, methyl radical reacts with CH_3I to produce C_2H_6, and the resulting iodine atom traps [Cp*Ir(bpy)]$^+$ to form $[\mathbf{4}]^+$. Though the products of these simplified mechanisms are indistinguishable, reactions from intermediate species can differentiate the two pathways.

Scheme 2. Pathways for Ethane Production from $[\mathbf{2}]^+$

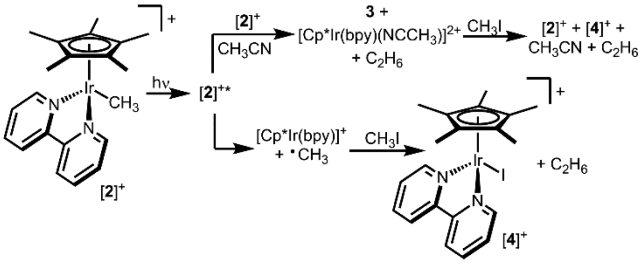

Preliminary reactions gave indications of an intermediate methyl radical. In addition to CH_4, partially deuterated CH_3D was formed (eq 2) along with the distinctive 1:2:3:2:1 pentet (J_{HD} = 1.1 Hz) indicative of propionitrile isotopologue CH_3CD_2CN (eq 3). Both results indicate $D^•$ abstraction from the solvent CD_3CN, which is a thermodynamically favorable reaction for $^•CH_3$ (*vide infra*). Attempts were made to examine the solvent decomposition specifically, but photolysis in the absence of added substrate produced an intractable mixture of products, as occurs for $[\mathbf{1}]^+$.

$$^•CH_3 + CD_3CN \rightarrow CH_3D + {}^•CD_2CN \tag{2}$$

$$^•CD_2CN + CH_3I \rightarrow I^• + CH_3CD_2CN \tag{3}$$

If ethane formation follows a self-quenching mechanism, then ethane, **3**, and $[Cp^*Ir(bpy)(NCCH_3)]^{2+}$ would likely be the initial products, according to the top pathway of Scheme 2. We have shown that acetic acid (AcOH) will readily protonate reduced **3** to form $[\mathbf{1}]^+$.[8,21] In the presence of AcOH then, a reaction following a self-quenching pathway would be expected to initially form ethane and then form H_2 as $[\mathbf{1}]^+$ formed *in situ* reacts. Irradiation of [**2**][PF_6] in the presence of excess AcOH produced CH_4 and CH_3D, observed by ^1H NMR and GC headspace analysis (Figure S18). Methane was detected in 50% yield. However, only trace amounts of ethane were observed by ^1H NMR spectroscopy and headspace GC analysis, and H_2 was not detected. The primary Ir-containing product was [Cp*Ir(bpy)(OAc)]$^+$ (86%). The absence of propionitrile in this reaction and in the reaction with CH_3OTs suggests that propionitrile is formed from a reaction between activated solvent and CH_3I (eq 3). Detecting neither H_2 nor hydride $[\mathbf{1}]^+$ suggests that Ir(I) complex **3** is not produced *in situ.*

Evidence for a Radical-Based Mechanism. To investigate the mechanism of ethane formation, unlabeled [Cp*Ir(bpy)($^{12}CH_3$)][PF_6] was photolyzed in the presence of labeled $^{13}CH_3I$. Methyl group parentage was tracked by ^1H NMR spectroscopy over the course of a 30 min photolysis of [**2**][PF_6] and $^{13}CH_3I$ with 443 nm light in CD_3CN. In that period, 20% of methyl $[\mathbf{2}]^+$ had reacted to form iodide $[\mathbf{4}]^+$. During photolysis, $^{12}CH_3$ scrambled into the methyl iodide at approximately the same rate as $[\mathbf{2}]^+$ was consumed, but only a small amount (1%) of isotopic enrichment of the methyl group of $[\mathbf{2}]^+$ was observed. No isotopic scrambling was observed in the dark.

These scrambling rates are telling of the initial steps in the reaction (Scheme 3). If Ir(I) complex **3** were formed in the course of the reaction and methyl $[\mathbf{2}]^+$ were regenerated by methyl iodide (as in Scheme 2, top), then $^{13}CH_3$ would be expected to be incorporated into $[\mathbf{2}]^+$ at half the rate at which $[\mathbf{2}]^+$ is consumed. The observed rates fit a mechanism in which initial cleavage of the Ir−$^{12}CH_3$ bond produces a radical pair that can either separate or recombine. Once separated, the $^{12}CH_3$ radical reacts with $^{13}CH_3I$ to form $^{13}CH_3$ radical, which becomes the dominant radical carrier because of the high

Scheme 3. Initial Steps of Isotope Scrambling

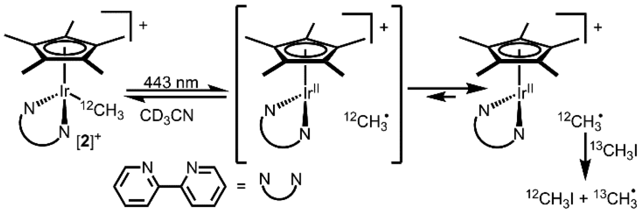

concentration of $^{13}CH_3I$. Termination of free methyl radical with $[Cp^*Ir(bpy)]^{2+}$ must be rare to account for the minimal ^{13}C enrichment of $[\mathbf{2}]^+$.

The dominance of $^{13}CH_3$ radical as the primary radical carrier in solution is also seen in the distribution of organic products. Because of the complex ^1H NMR splitting pattern of $^{12}CH_3{}^{13}CH_3$ and overlapping peaks from different isotopologues,[22] precise quantification of the ethane distribution was untenable. Integration of the satellites gives the total concentration of ^{13}C incorporated in ethane either in $^{12}CH_3{}^{13}CH_3$ or $^{13}CH_3{}^{13}CH_3$ (Figure 4, closed squares) while the center peak gives ^{12}C concentration in $^{12}CH_3{}^{13}CH_3$ or $^{12}CH_3{}^{12}CH_3$ (Figure 4, open squares). Because this treatment is counting carbons individually, the ethane concentration is half the sum of the two measurements. About 5 times as much ^{13}C is incorporated into ethane as ^{12}C. Consistent with this, $^{13}CH_4$ and $^{13}CH_3D$ were generated at a faster rate than $^{12}CH_4$ and $^{12}CH_3D$. These results suggest that the methyl radical that forms on irradiation undergoes nonproductive radical reactions with the excess of $^{13}CH_3I$ before forming methane or ethane.

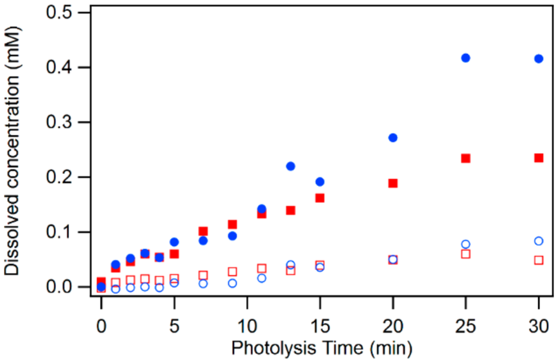

Figure 4. Time course of dissolved methane and ethane during photolysis of $[\mathbf{2}]^+$ and $^{13}CH_3I$ in CD_3CN, showing that incorporation of ^{13}C into organic products outpaces that of ^{12}C. $^{13}CH_4$ and $^{13}CH_3D$ (closed red squares), $^{12}CH_4$ and $^{12}CH_3D$ (open red squares), ^{13}C in ethane (closed blue circles), and ^{12}C in ethane (open blue circles).

Radical probes were employed to provide further evidence for the presence of free radicals during photolysis. Photolysis of 5.6 mM $[\mathbf{2}]^+$ and 12 mM CH_3I in CD_3CN was carried out with 443 nm light for 90 min in the presence of 24 mM radical trap TEMPO (Scheme 4). Irradiation exclusively produced TEMPO−CH_3 to the exclusion of methane and ethane. The iridium product was $[\mathbf{4}]^+$, which was formed at half the rate at which TEMPO−CH_3 appeared (Figure 5). Ir−CH_3 homolysis will produce 1 equiv of TEMPO−CH_3 and $[Cp^*Ir(bpy)]^+$. To account for rates and electrons, the Ir(II) complex must cleave CH_3I to form an additional equivalent of TEMPO−CH_3 and the final species $[\mathbf{4}]^+$.

Scheme 4. Reaction with Radical Trap TEMPO

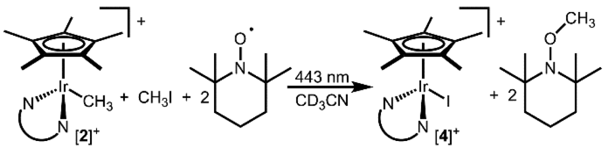

An intramolecular alkyl radical clock was also synthesized to probe radical intermediates. 5-Hexenyl radical is known to quickly cyclize to form cyclopentylmethyl radical.[23] To access this radical clock, excess 6-bromo-1-hexene was added to a purple solution of Ir(I) complex **3** in Et_2O and allowed to stir in the dark for 4 days. Over that time, a yellow solid precipitated from solution and was isolated by filtration and washed with ether giving $[Cp^*Ir(bpy)((CH_2)_4CHCH_2)][Br]$ ($[\mathbf{5}][Br]$).

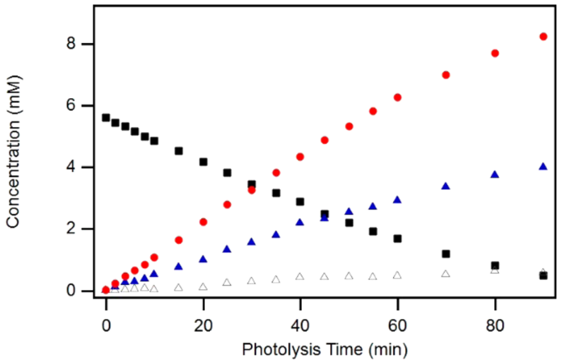

Figure 5. Concentrations from ^1H NMR spectroscopy following the irradiation at 443 nm of a solution of 5.6 mM $[\mathbf{2}][PF_6]$ (black squares), 12 mM CH_3I, and 24 mM TEMPO in CD_3CN. TEMPO−CH_3 (red circles) grows in at twice the rate of iodide $[\mathbf{4}]^+$ (blue triangles). The decrease in $[CH_3I]$ (not shown) accounts for half of the methyl of TEMPO−CH_3. Methyl $[\mathbf{2}]^+$ is consumed at a slightly faster rate than that at which $[\mathbf{4}]^+$ appears; a minor iridium (open triangles, 10%) containing species grows in as evidence of a side reaction.

Irradiation of a solution of $[\mathbf{5}][Br]$ in CD_3CN gave methylcyclopentane (confirmed by spiking with an authentic sample), 1,5-hexadiene, and methylenecyclopentane (Scheme 5). The Ir products were **3**, $[Cp^*Ir(bpy)(Br)]^+$ and a new minor species. ESI-MS of the product mixture showed a peak at $m/z = 567.23452$. This is the same mass as the starting material $[\mathbf{5}]^+$ (calcd $m/z = 567.2351$), but NMR data showed that the starting material was fully consumed (Figure S21). The same mass would also be consistent with ring-closed product $[Cp^*Ir(bpy)(CH_2C_5H_9)]^+$ (included in gray in Scheme 5 because it was not fully characterized).

Scheme 5. Reaction of Radical Clock Complex [5][Br]

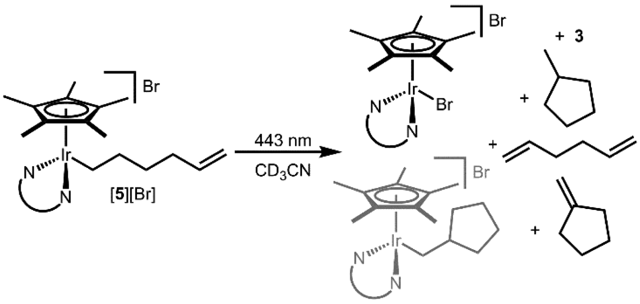

The presence of methylcyclopentane in the product mixture is evidence for the homolysis of the Ir−C bond. The ring-closed cyclopentylmethyl radical formed after homolysis could (a) recombine with Ir(II) to form $[Cp^*Ir(bpy)(CH_2C_5H_9)]^+$, (b) lose $H^\bullet$ to form methylenecyclopentane, or (c) gain $H^\bullet$ to form methylcyclopentane. 1,5-Hexadiene is formed by $H^\bullet$ abstraction by $[Cp^*Ir^{II}(bpy)]^+$ from the formed 5-hexenyl radical before ring closure. This process produces $[Cp^*Ir^{III}(bpy)(H)]^+$ ($[\mathbf{1}]^+$) which can supply the additional H atom equivalent need to form methylcyclopentane. Formation of the final Ir(I) and Ir(III) products could be formed by disproportionation of [Cp*Ir(bpy)]$^+$. Similar mechanisms for light-induced β-hydride elimination have been previously proposed on Ir,[24] and this is a common mechanism in cobalt alkyl photochemistry.[25,26]

Differentiating Mechanisms with Excited State Lifetime and Kinetic Order. Ir−C bond homolysis could occur through either monometallic homolysis from the excited state (Scheme 1, blue) or following an electron transfer which weakens the Ir−CH_3 bonds (Scheme 1, black). Excited state lifetimes and kinetic order were investigated to determine which of these pathways was operative.

Excited state lifetimes and luminescence quantum yields were investigated to look for self-quenching directly (see Supporting Information for full details). No change in photoluminescent quantum yield was observed in the range of 0.02−0.6 mM of [**2**]$^+$. The lifetime of [**2**]$^{+*}$ was found to be 50 ns by time-correlated single photon counting, with no dependence on [**2**]$^+$ in the range of 0.02−0.9 mM. Both results indicate that [**2**]$^{+*}$ is not efficiently quenched by [**2**]$^+$. Quenching by methyl iodide ($E_{1/2}$ = −2.18 V)[27] was also investigated; no change in lifetime was observed to 1 M CH_3I.

The reaction of [**2**]$^+$ and CH_3I in CH_3CN during irradiation with 443 nm light was also monitored by UV−vis spectroscopy in quartz cuvettes. The disappearance of the MLCT feature of [**2**]$^+$ was monitored at 443 nm, and quantum yields for the disappearance of [**2**]$^+$ were calculated over the course of 10% consumption. Samples which were photolyzed until no further change occurred were consistent with the spectrum of [**4**]$^+$ (Figure S25).

Order in Ir was determined by monitoring the disappearance of [**2**][PF_6] in an irradiated quartz cuvette in the presence of 0.1 M CH_3I in CH_3CN. The quantum yield for consumption of starting material remained constant at 1.0(1)% from 0.08 to 0.28 mM [**2**]$^+$ (Figure 6). Because calculating quantum yield includes normalization for sample absorbance, a lack of dependence on the chromophore concentration indicates an overall first-order dependence on chromophore [**2**]$^+$. Order in CH_3I was determined by varying the concentration of substrate from 0.02 to 0.3 M at constant concentration of [**2**]$^+$. No dependence of quantum yield on substrate concentration was observed, indicating that the reaction is zero-order in CH_3I.

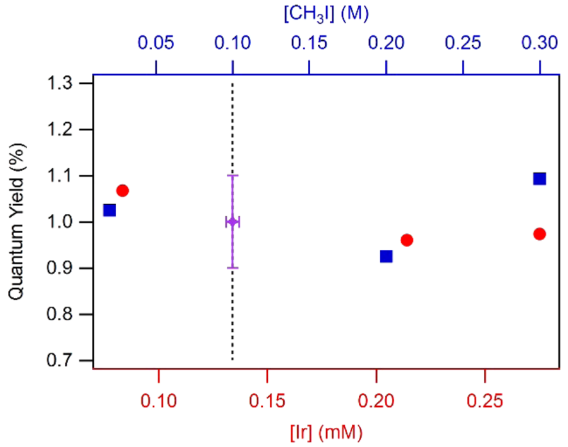

Figure 6. Dependence of quantum yield on [CH_3I] (blue squares) and [[**2**]$^+$] (red circles) in CH_3CN photolyzed with 443 nm light. The dashed line marks the constant concentrations of CH_3I and [**2**]$^+$ (0.1 M and 0.13 mM, respectively) held while the other reagent varied. The purple point is 4 independent trials under the same conditions with error given by one standard deviation. The lack of dependence on CH_3I indicates the reaction is zero-order in substrate, while the lack of dependence on [**2**]$^+$ indicates an overall first-order reaction as [**2**]$^+$ is the chromophore.

Order in Ir and substrate was similarly investigated for the reaction of [**2**]$^+$ in the presence of AcOH to probe the reaction with a different substrate. Variation of [**2**]$^+$ concentration from 0.8 to 0.21 mM in the presence of a constant concentration of 0.1 M AcOH in CH_3CN resulted in no change in quantum yield (1.7(3)%, Figure S27). To probe higher iridium concentrations, solutions of 1−8 mM [**2**]$^+$ in CD_3CN and 0.1 M AcOH were irradiated in standard NMR tubes with 443 nm light and monitored by ^1H NMR spectroscopy. No change in quantum yield was observed (Figure S28). Varying [AcOH] caused no change in quantum yield, indicating a zero-order dependence on substrate.

Additionally, if a bimolecular reaction of two cationic iridium species was occurring, then one might expect an increase in quantum yield on addition of electrolyte. Quantum yields for the disappearance of [**2**]$^+$ with and without 0.1 M [^{n}Bu$_4$N]-[PF_6] were identical in four trials with concentrations of [**2**]$^+$ at 0.07 and 0.18 mM with 0.05 M AcOH acid, indicating that the reaction does not involve the close approach of two charged species.

From a kinetic analysis indicating that the reaction is first-order in [**2**]$^+$ and zero-order in substrate, several characteristics of the reaction become apparent. The first is that bimolecular self-quenching cannot play a significant role in the reaction. The second is that reactions involving the added organic methyl source must occur after the rate-determining step. Additionally, the radical chain is not significantly propagated through radical attack on [**2**]$^+$ to produce either Ir(II) or methyl radical. Such a process would result in an additional pathway to consuming [**2**]$^+$ and typically results in $^3/_2$-order in [**2**]$^+$.[28]

Many of the species that would be formed to continue propagation of methyl radical in solution, ICH_2CN and I_2, have particularly weak bonds (44.7 and 36.4 kcal·mol^{-1}, respectively)[29] and are unlikely to be generated in high concentrations. Indeed, attempts to detect ICH_2CN by photolyzing a solution of [**2**][PF_6] with excess CH_3I in 9:1 CH_3CN/CD_3CN produced no iodoacetonitrile and no ethane by ^1H NMR spectroscopy. Instead, evidence for another C−C bond forming event was observed: 0.5 equiv of succinonitrile ($(CH_2CN)_2$) was detected per [**2**]$^+$, presumably produced by the termination of two acetonitrile radicals. Given that iodide [**4**]$^+$ was formed in this reaction as well, CH_3I must be involved in other radical reactions; therefore, short chain reactions must occur.

To assess the presence of succinonitrile, liquid-phase GC/MS was undertaken on the solution resulting from photolysis of 6 mM [**2**][PF_6] and 45 mM CH_3I in CH_3CN and in CD_3CN. In CH_3CN, 2.6 mM succinonitrile was produced, while in CD_3CN, only 0.1 mM succinonitrile-d_4 was produced. The absence of ethane in CH_3CN suggests that the slightly more inert C−D bond of CD_3CN encourages ethane formation. Given the difference in product distribution in *protio* and *deutero* solvent, we investigated the quantum yield for the reaction of [**2**]$^+$ in CD_3CN with CD_3I and found no decrease. Therefore, the isotope effect is product-determining but not rate-determining. Either initial homolysis or solvent separation of the radical pair is likely the rate-determining step.

Understanding the Preference for Homolysis. The collected data indicate that ethane and methane production occur following monometallic Ir−CH_3 bond homolysis from the excited state. Bond dissociation enthalpies relevant to this discussion are collected in Table 2. Deuterium atom abstraction by $^{\bullet}CH_3$ from CD_3CN forms CH_3D. Methyl radical is thermodynamically capable of abstracting a hydrogen atom from acetonitrile.[29] The absence of propionitrile in reactions with AcOH and CH_3OTs suggests that propionitrile-d_2 results from the reaction of $^{\bullet}CD_2CN$ with CH_3I. Ethane could be formed either in a reaction of $^{\bullet}CH_3$ with CH_3I or in a termination step upon recombination of two methyl radicals. Addition of $I^{\bullet}$ to the primary Ir photoproduct $[Cp^*Ir^{II}(bpy)]^+$ offers an organometallic termination pathway that affords the observed iodide complex.

Table 2. Relevant Bond Dissociation Energies

molecule	ΔH (kcal·mol^{-1})	ref
H−H	104.2	29
H−CH_3	105	29
H−CH_2CN	97	29
I−CH_3	57	29
I−CH_2CN	44.7	29
I−I	36.4	29
H_3C−CH_2CN	83.2	29
$NCCH_2$−CH_2CN	70.6	30
H−Ir(Cp*)(PMe_3)(H)	74	31
H_3C−Ir(Cp*)(PMe_3)(CH_3)	56	31

To better understand the mechanism change from electron transfer with $[\mathbf{1}]^+$ to homolysis with $[\mathbf{2}]^+$, relevant thermodynamic parameters were considered. One possibility is that homolysis of an Ir−CH_3 bond is thermodynamically favorable relative to homolysis of an Ir−H bond. While the hydrogen atom and methyl radical are almost equally stable (ΔH(H−H) = 104 kcal·mol^{-1}; ΔH(H_3C−H) = 105 kcal·mol^{-1}),[29] the bond dissociation enthalpies of Ir−H in $[\mathbf{1}]^+$ and Ir−CH_3 in $[\mathbf{2}]^+$ may be very different. The most similar system for which M−CH_3 and M−H bond strengths have been measured is Cp*Ir(PMe_3)X_2 (where X = H and CH_3). In this system, ΔH(Ir−H) = 74 kcal·mol^{-1}, while ΔH(Ir−CH_3) = 56 kcal·mol^{-1}. This ∼20 kcal·mol^{-1} decrease in bond dissociation enthalpy from ΔH(Ir−H) to ΔH(Ir−CH_3) is consistent with other Ir systems in which both have been measured.[31] This is a considerable difference, especially when considered in light of the overall similarity of $[\mathbf{1}]^+$ and $[\mathbf{2}]^+$.

Homolysis is also consistent with the nature of the orbitals involved in the MLCT transition. The largest contribution to the excitation depopulates a σ bond between Ir and CH_3 (HOMO, Figure 3C). Irradiation of this transition would, therefore, be expected to weaken the Ir−C bond.

While a more accessible homolysis pathway explains much of the observed chemistry, the differences in quantum yields for $[\mathbf{1}]^+$ and $[\mathbf{2}]^+$ suggest that there may be other factors. The quantum yields for conversion of $[\mathbf{2}]^+$ are low, especially when compared with quantum yields for H_2 evolution for $[\mathbf{1}]^+$ that approach unity. Homolysis may be out-competing electron transfer, and low quantum yields could be a result of efficient recombination from the radical pair. Alternatively, the discrepancy may be explained by an inaccessible self-quenching process. As discussed above, self-quenching for $[\mathbf{2}]^{+*}$ and $[\mathbf{2}]^+$ lies 9 kcal·mol^{-1} uphill. This is a larger barrier than that for $[\mathbf{1}]^{+*}$ and $[\mathbf{1}]^+$ (3 kcal·mol^{-1}) and may, indeed, be insurmountable even with a following reaction. Such self-quenching reactions are often kinetically limited as well. Self-quenching of $[Ru(bpy)_3]^{2+}$ with its excited state is thermodynamically favorable, but only occurs when suitable electron donors and acceptors are included in solution.[32,33] In the absence of a viable electron transfer pathway for $[\mathbf{2}]^+$, homolysis provides a feasible pathway to dissipate the energy of the excited state.

■ CONCLUSIONS

A new iridium methyl complex, $[Cp^*Ir(bpy)(CH_3)]^+$, was prepared and characterized. Photolysis of this complex in the presence of CH_3I forms C−C bonds; ethane, propionitrile, and succinonitrile are all formed. The mechanism of C−C bond formation was shown to proceed through monometallic radical homolysis, rather than the bimetallic electron transfer mechanism that led to H−H bond formation from $[\mathbf{1}]^+$. The minor structural change of substituting a methyl ligand for a hydride ligand, despite modifying the electrochemical and photophysical properties of the molecule only slightly, was sufficient to give rise to drastically different reactivity. Comparison of the bond dissociation enthalpies of similar complexes suggests that the mechanism change can be explained by the weaker Ir−CH_3 bond in comparison to the Ir−H bond. The dramatic differences underscore the changes in reactivity that can be observed on minor synthetic variation.

■ EXPERIMENTAL SECTION

General Considerations. Procedures were carried out under nitrogen except where noted. All solutions containing metal methyl species were protected from ambient light during preparation to prevent excited state reactions. All reagents were commercially available and used without further purification. Organic solvents were dried and degassed with argon using a Pure Process Technology solvent system. Deuterated solvents were purchased from Cambridge Isotope Laboratories, Inc. and degassed with three freeze−pump−thaw cycles before storing over sieves in a N_2 glovebox. UV−vis spectra were obtained using an Ocean Optics USB2000+ spectrometer with a DTMINI-2GS deuterium/tungsten halogen light source controlled by OceanView software. NMR spectra were obtained on 400, 500, or 600 MHz spectrometers. ^1H and ^{13}C NMR spectra were referenced to the residual solvent signals. Spectra were processed using the MestReNova software suite from Mestrelab Research S. L. Mass spectrometry was carried out with an LTQ FT (ICR 7T) (ThermoFisher, Bremen, Germany) mass spectrometer. Samples (in acetonitrile solution) were introduced via a microelectrospray source at a flow rate of 3 μL/min. Xcalibur (ThermoFisher, Breman, Germany) was used to analyze the data. Molecular formula assignments were determined with Molecular Formula Calculator (v 1.2.3). For ICP-MS, samples were prepared in 2% nitric acid solution diluted with 18.2 MΩ/cm water and were analyzed with an Element XR inductively coupled plasma (ThermoFisher, Bremen, Germany) mass spectrometer (ICP-MS). Samples were introduced via a peristaltic pump connected to an Elemental Scientific SC autosampler (Omaha, Nebraska). Iridium 193 was monitored in low-resolution mode for 30 s for each sample (∼300 scans). For succinonitrile detection, the chromatographic separation and detection were performed on an Exactive GC system (ThermoFisher Scientific, Breman, Germany) equipped with a Trace 1300 SSL injector and TriPlus RSH autosampler with a TRACE TG-5SILMS column and He carrier gas (purity 99.999%). The mass spectrometer was operated in full scan mode using positive mode chemical ionization (PCI, UHP Methane gas) with a mass range of 40−600 m/z. The instrumental control, data acquisition, and data processing were performed with Thermo's Xcalibur and TraceFinder software packages. All UV−vis and photoluminescence samples were prepared in an N_2 glovebox in 1 cm path length 4-sided quartz cuvettes, sealed with screwcaps, and reinforced with parafilm on removing from the glovebox, unless otherwise noted. Single-crystal XRD data were collected on a Bruker APEX-II CCD diffractometer at 100 K with Cu Kα radiation (λ = 1.54175 Å). Using Olex2,[34] the structures were solved with the olex2.solve[35] structure solution program using Charge Flipping and refined with the XL[36] refinement program using least-squares minimization. The complex Cp*Ir(bpy) was prepared following literature procedures.[37] Elemental analyses were performed by Robertson Microlit Laboratories (Ledgewood, NJ).

Electrochemistry. Cyclic voltammograms were measured with glassy carbon working electrodes (polished with 0.3 and 0.05 μm alumina powder before use), platinum wire counter electrodes, and a Ag pseudoreference electrode. An undivided cup cell was used. Experiments were carried out in an N_2 filled glovebox using a Pine WaveNow potentiostat controlled by Aftermath software connected to a computer outside of the glovebox by a custom USB feed through. Ferrocene was added at the end of data collection, and all potentials are reported relative to the $Fc^{0/+}$ couple.

Photoluminescence Studies. Steady-state emission and excitation spectra were recorded at room temperature on a Photon Technology, Inc. Quantamaster 4SE-NIR5 spectrometer PC-controlled by FelixX32 software. Excitation light was provided by a 75 W xenon light source coupled to a single monochromator outfitted with a 1200 L/mm grating blazed at 400 nm. A 300 nm long pass filter was placed before the sample to prevent deep UV excitation from a second-order grating effect. Emission was collected at a right angle relative to excitation, focused into a single monochromator (grating blazed at 500 nm with 1200 L/mm) and detected by a Hamamatsu R928P photomultiplier tube used in single photon counting mode. Slit widths for both emission and excitation monochromators were fixed at 0.5 mm. All spectra were corrected for system response.

Absolute photoluminescence quantum yield was measured on an Edinburgh FLS-920 emission spectrophotometer with detection by a Hamamatsu R2658P photomultiplier tube to count photons to 950 nm by which wavelength the phosphorescence had decayed to zero. Photoluminescent lifetimes were measured by time-correlated single photon counting on the Edinburgh instrument with excitation by a 443 nm, 73.3 ps width laser.

Synthesis. _[Cp*Ir(bpy)(CH$_3$)][I] ([**2**][I])._ A slight excess of a 50 mM solution of CH_3I in Et_2O (3.30 mL, 0.165 mmol) was added dropwise to a stirring saturated purple solution of Cp*Ir(bpy) (56.6 mg, 0.117 mmol). A fluffy yellow solid precipitated over the course of several minutes. The solid was separated by filtration and washed with Et_2O resulting in 67.6 mg of air-stable [**2**][I] (0.108 mmol, 92% yield, >99% pure by ^1H NMR and EA). Single crystals for XRD were grown by vapor diffusion of Et_2O into a solution of [2][I] in CH_3CN. Characterization obtained of the original precipitate: ^1H NMR (600 MHz, CD_3CN) δ 8.67 (ddd, J = 5.8, 1.5, 0.8 Hz, 2H), 8.43 (dt, J = 8.2, 1.1 Hz, 2H), 8.08 (ddd, J = 8.1, 7.5, 1.5 Hz, 2H), 7.60 (ddd, J = 7.4, 5.7, 1.4 Hz, 2H), 1.68 (s, 15H), −0.04 (s, 3H). $^{13}C\{^1H\}$ NMR (151 MHz, CD_3CN) δ 156.01, 152.44, 139.08, 129.00, 125.32, 90.85, 8.70, −6.35. $\lambda_{abs,max}$ (CH_3CN) = 418 nm. HRMS (ESI$^+$) [**2**]$^+$ Calcd for $C_{21}H_{26}IrN_2$: 499.17258. Found 499.17310. Anal. Calcd for $C_{21}H_{26}IIrN_2$: C, 40.32; H, 4.19; N, 4.48. Found: C, 40.49; H, 4.12; N, 4.33.

[Cp*Ir(bpy)(CH$_3$)][PF$_6$] ([**2**][PF$_6$]). In air, complex [**2**][I] (54.1 mg, 0.086 mmol) was dissolved in 75 mL of 9:1 H_2O/CH_3OH. Excess [NH_4][PF_6] (160 mg) was added as a solid, resulting in the immediate precipitation of a fine yellow solid. The solid was separated by filtration through a fine frit and flushed with water resulting in 49.8 mg of [**2**][PF_6] (0.077 mmol, 89% yield, >99% pure by ^1H NMR and EA). ^1H NMR (600 MHz, CD_3CN) δ 8.67 (d, J = 5.7 Hz, 2H), 8.43 (d, J = 8.1 Hz, 2H), 8.08 (t, J = 7.8 Hz, 2H), 7.60 (t, J = 6.6 Hz, 2H), 1.68 (s, 15H), −0.04 (s, 3H). $^{13}C\{^1H\}$ NMR (151 MHz, CD_3CN) δ 156.01, 152.45, 139.07, 129.00, 125.33, 90.85, 8.70, −6.36. Anal. Calcd for $C_{21}H_{26}F_6IrN_2P$: C, 39.19; H, 4.07; N, 4.35. Found: C, 38.94; H, 3.89; N, 4.15.

[Cp*Ir(bpy)(I)]$^+$ ([**4**]$^+$). [Cp*Ir(bpy)(I)]$^+$ was prepared by addition of 3 equiv of NaI to 3.9 mg of [Cp*Ir(bpy)(OH_2)][OTf]$_2$ in CD_3CN. ^1H NMR (500 MHz, CD_3CN) δ 8.88 (d, J = 5.7 Hz, 2H), 8.46 (d, J = 8.1 Hz, 2H), 8.18 (t, J = 8.1 Hz, 2H), 7.75−7.71 (m, 2H), 1.74 (s, 15H). $\lambda_{abs,max}$ (CH_3CN) = 375 nm (2500 M^{-1} cm^{-1}).

[Cp*Ir(bpy)((CH$_2$)$_4$CHCH$_2$)][Br] ([**5**][Br]). To a purple stirring solution of Cp*Ir(bpy) (28.4 mg, 0.059 mmol) in Et_2O was added 10 equiv of 6-bromo-1-hexene (79 μL, 0.59 mmol). The solution was allowed to stir for 4 days, during which a yellow solid precipitated, which was filtered to separate and washed 3 times with ether giving 34.2 mg of [**5**][Br] (0.053 mmol, 90% yield, 96% pure by ^1H NMR). ^1H NMR (600 MHz, CD_3CN) δ 8.65 (ddd, J = 5.8, 1.5, 0.8 Hz, 2H), 8.47 (dt, J = 8.0, 1.1 Hz, 2H), 8.11−8.07 (m, 2H), 7.60 (ddd, J = 7.4, 5.7, 1.4 Hz, 2H), 5.63−5.49 (m, 1H, Ir-$CH_2CH_2CH_2CH_2\boldsymbol{CH}CH_2$), 4.79−4.71 (m, 2H, Ir-$CH_2CH_2CH_2CH_2CH\boldsymbol{CH_2}$), 1.71 (tdd, J = 8.1, 6.2, 1.4 Hz, 2H, Ir-$CH_2CH_2CH_2\boldsymbol{CH_2}CHCH_2$), 1.65 (s, 15H), 0.97 (p, J = 6.9 Hz, 2H, Ir-$CH_2CH_2\boldsymbol{CH_2}CH_2CHCH_2$), 0.83−0.72 (m, 4H, Ir-$\boldsymbol{CH_2CH_2}CH_2CH_2CHCH_2$). $^{13}C\{^1H\}$ NMR (151 MHz, CD_3CN) δ 155.93, 152.13, 139.98 (Ir-$CH_2CH_2CH_2CH_2\boldsymbol{CH}CH_2$), 138.59, 128.53, 125.00, 114.47 (Ir-$CH_2CH_2CH_2CH_2CH\boldsymbol{CH_2}$), 90.93, 33.91 (Ir-$CH_2CH_2\boldsymbol{CH_2}CH_2CHCH_2$), 33.73 (Ir-$CH_2CH_2CH_2\boldsymbol{CH_2}CHCH_2$), 30.53 (Ir-$CH_2\boldsymbol{CH_2}CH_2CH_2CHCH_2$), 13.44 (Ir-$\boldsymbol{CH_2}CH_2CH_2CH_2CHCH_2$), 8.19. HRMS (ESI$^+$) [**5**]$^+$ Calcd for $C_{26}H_{34}IrN_2$: 567.23522. Found: 567.23542.

Representative Photolysis Monitored by ^{1}H NMR Spectroscopy. In a nitrogen-filled glovebox, 4.8 mg of [**2**][PF_6] was dissolved in 1 mL of CD_3CN. Then, 0.98 mL of this solution was transferred to a vial containing 6 μL of CH_3I, and 20 μL of a 150 mM mesitylene solution in filtered CD_3CN was added as an internal standard. The solution was split between two screw cap NMR tubes. ^1H NMR spectra were recorded after removing the tubes from the glovebox and reinforcing the seal with parafilm. One tube remained wrapped in aluminum foil, while the other was irradiated with 443 nm light (Thor Multichannel) until [**2**]$^+$ had fully reacted. Using a gastight, locking syringe, 0.3 mL of the headspace was removed and analyzed by GC to determine yields of methane and ethane

Representative Photolysis Monitored by UV−Vis Spectroscopy. Samples for analysis by UV−vis spectroscopy were typically prepared in sets of 4. In a nitrogen-filled glovebox, excess CH_3CN was filtered through a pipet filter to remove sieve dust from storage. Stock solutions of [**2**][PF_6] and CH_3I were prepared and delivered to the cuvettes with volumetric syringes. The total volume of solution was brought to 2 mL by addition of CH_3CN. After capping with screwcap, the samples were removed from the glovebox, parafilmed around the cap, and stored in the dark. Samples were photolyzed sequentially. Each was irradiated in 30 s segments (Thor Multichannel, 2.37×10^{-6} moles of photons min^{-1}, determined by chemical actinometry)[8] followed by collection of a UV−vis spectrum. Samples were photolyzed for a total of 3 min.

Computational Methods. Geometry optimizations, frequency, and time-dependent calculations were done using the hybrid functional M06 as implemented in Gaussian 09[38] with the LANL2DZ ECP basis set[39,40] for the iridium atom and 6-311G** for all other atoms. The PCM implicit solvation models (CH_3CN solvent) was employed for all calculations. This strategy has been effective for Ir TD-DFT in the literature.[41,42] Calculations were analyzed using the Chemcraft suite.

■ ASSOCIATED CONTENT

Ⓢ Supporting Information

The Supporting Information is available free of charge on the ACS Publications website at DOI: 10.1021/acs.organomet.7b00175.

NMR spectra, additional experimental details, crystallographic and computational details (PDF)

Text file of [**2**]$^+$ computed molecule Cartesian coordinates in a format for convenient visualization (XYZ)

Accession Codes

CCDC 1545750 and 1545751 contain the supplementary crystallographic data for this paper. These data can be obtained free of charge via www.ccdc.cam.ac.uk/data_request/cif, or by emailing data_request@ccdc.cam.ac.uk, or by contacting The Cambridge Crystallographic Data Centre, 12, Union Road, Cambridge CB2 1EZ, UK; fax: +44 1223 336033.

AUTHOR INFORMATION

Corresponding Author

*E-mail: ajmm@email.unc.edu.

ORCID

Catherine L. Pitman: 0000-0003-2094-8280

Alexander J. M. Miller: 0000-0001-9390-3951

Notes

The authors declare no competing financial interest.

ACKNOWLEDGMENTS

We gratefully acknowledge funding from the Division of Chemical Sciences, Geosciences & Biosciences, Office of Basic Energy Sciences, U.S. Department of Energy through Grant DE-SC0014255. C.L.P. is a Fellow of the Royster Society. This research made use of instrumentation funded by the UNC EFRC: Center for Solar Fuels, an Energy Frontier Research Center supported by the U.S. Department of Energy, Office of Science, Office of Basic Energy Sciences, under award number DE-SC0001011. We thank B. Ehrmann for help with GC-MS, L. Gregor for help with ICP-MS, K. Brereton for help with TD-DFT, and M. Chambers for helpful discussions.

REFERENCES

(1) Hill, R. H.; Puddephatt, R. J. *Organometallics* **1983**, *2*, 1472–1474.

(2) Alt, H. G. *Angew. Chem., Int. Ed. Engl.* **1984**, *23*, 766–782.

(3) Ravelli, D.; Protti, S.; Fagnoni, M. *Chem. Rev.* **2016**, *116*, 9850–9913.

(4) Paul, A.; Smith, M. D.; Vannucci, A. K. *J. Org. Chem.* **2017**, *82*, 1996–2003.

(5) Geoffroy, G. L.; Wrighton, M. S. *Organometallic Photochemistry*; Academic Press: New York, 1979.

(6) Brown, S. H.; Crabtree, R. H. *J. Am. Chem. Soc.* **1989**, *111*, 2946–2953.

(7) van Slageren, J.; Klein, A.; Záliš, S. *Coord. Chem. Rev.* **2002**, *230*, 193–211.

(8) Chambers, M. B.; Kurtz, D. A.; Pitman, C. L.; Brennaman, M. K.; Miller, A. J. M. *J. Am. Chem. Soc.* **2016**, *138*, 13509–13512.

(9) Groom, C. R.; Bruno, I. J.; Lightfoot, M. P.; Ward, S. C. *Acta Crystallogr., Sect. B: Struct. Sci., Cryst. Eng. Mater.* **2016**, *72*, 171–179.

(10) Dadci, L.; Elias, H.; Frey, U.; Hoernig, A.; Koelle, U.; Merbach, A. E.; Paulus, H.; Schneider, J. S. *Inorg. Chem.* **1995**, *34*, 306–315.

(11) Abura, T.; Ogo, S.; Watanabe, Y.; Fukuzumi, S. *J. Am. Chem. Soc.* **2003**, *125*, 4149–4154.

(12) Lenges, C. P.; White, P. S.; Marshall, W. J.; Brookhart, M. *Organometallics* **2000**, *19*, 1247–1254.

(13) Nakai, H.; Jeong, K.; Matsumoto, T.; Ogo, S. *Organometallics* **2014**, *33*, 4349–4352.

(14) Blakemore, J. D.; Hernandez, E. S.; Sattler, W.; Hunter, B. M.; Henling, L. M.; Brunschwig, B. S.; Gray, H. B. *Polyhedron* **2014**, *84*, 14–18.

(15) Irwin, M.; Doyle, L. R.; Krämer, T.; Herchel, R.; McGrady, J. E.; Goicoechea, J. M. *Inorg. Chem.* **2012**, *51*, 12301–12312.

(16) Suenobu, T.; Guldi, D. M.; Ogo, S.; Fukuzumi, S. *Angew. Chem., Int. Ed.* **2003**, *42*, 5492–5495.

(17) Clark, C. C.; Marton, A.; Meyer, G. J. *Inorg. Chem.* **2005**, *44*, 3383–3385.

(18) Sandrini, D.; Maestri, M.; Ziessel, R. *Inorg. Chim. Acta* **1989**, *163*, 177–180.

(19) Bock, C. R.; Connor, J. A.; Gutierrez, A. R.; Meyer, T. J.; Whitten, D. G.; Sullivan, B. P.; Nagle, J. K. *J. Am. Chem. Soc.* **1979**, *101*, 4815–4824.

(20) Chamberlain, L. R.; Rothwell, A. P.; Rothwell, I. P. *J. Am. Chem. Soc.* **1984**, *106*, 1847–1848.

(21) Barrett, S. M.; Pitman, C. L.; Walden, A. G.; Miller, A. J. M. *J. Am. Chem. Soc.* **2014**, *136*, 14718–14721.

(22) Alemany, L. B.; Malloy, T. B.; Nunes, M. M.; Zaibaq, N. G. *J. Mol. Struct.* **2012**, *1023*, 176–188.

(23) Griller, D.; Ingold, K. U. *Acc. Chem. Res.* **1980**, *13*, 317–323.

(24) Bradley, P.; Suardi, G.; Zipp, A. P.; Eisenberg, R. *J. Am. Chem. Soc.* **1994**, *116*, 2859–2868.

(25) Schrauzer, G. N.; Sibert, J. W.; Windgassen, R. J. *J. Am. Chem. Soc.* **1968**, *90*, 6681–6688.

(26) Debuigne, A.; Poli, R.; Jérôme, C.; Jérôme, R.; Detrembleur, C. *Prog. Polym. Sci.* **2009**, *34*, 211–239.

(27) Occhialini, D.; Daasbjerg, K.; Lund, H. *Acta Chem. Scand.* **1993**, *47*, 1100–1106.

(28) Espenson, J. H. *Chemical Kinetics and Reaction Mechanisms*, 2nd ed.; McGraw Hill: New York, 1981.

(29) Luo, Y. R. *Comprehensive Handbook of Chemical Bond Energies*; CRC Press: Boca Raton, FL, 2007.

(30) Afeefy, H. Y.; Liebman, J. F.; Stein, S. E. In *NIST Chemistry WebBook, NIST Standard Reference Database Number 69*; Linstrom, P. J., Mallard, W. G., Eds.; National Institute of Standards and Technology: Gaithersburg, MD, 2016.

(31) Simoes, J. A. M.; Beauchamp, J. L. *Chem. Rev.* **1990**, *90*, 629–688.

(32) Nagle, J. K.; Young, R. C.; Meyer, T. J. *Inorg. Chem.* **1977**, *16*, 3366–3369.

(33) Creutz, C.; Sutin, N. *J. Am. Chem. Soc.* **1977**, *99*, 241–243.

(34) Dolomanov, O. V.; Bourhis, L. J.; Gildea, R. J.; Howard, J. A. K.; Puschmann, H. *J. Appl. Crystallogr.* **2009**, *42*, 339–341.

(35) Bourhis, L. J.; Dolomanov, O. V.; Gildea, R. J.; Howard, J. A. K.; Puschmann, H. *Acta Crystallogr., Sect. A: Found. Adv.* **2015**, *71*, 59–75.

(36) Sheldrick, G. M. *Acta Crystallogr., Sect. A: Found. Crystallogr.* **2008**, *64*, 112–122.

(37) Pitman, C. L.; Brereton, K. R.; Miller, A. J. M. *J. Am. Chem. Soc.* **2016**, *138*, 2252–2260.

(38) Frisch, M. J.; Trucks, G. W.; Schlegel, H. B.; Scuseria, G. E.; Robb, M. A.; Cheeseman, J. R.; Scalmani, G.; Barone, V.; Mennucci, B.; Petersson, G. A.; Nakatsuji, H.; Caricato, M.; Li, X.; Hratchian, H. P.; Izmaylov, A. F.; Bloino, J.; Zheng, G.; Sonnenberg, J. L.; Hada, M.; Ehara, M.; Toyota, K.; Fukuda, R.; Hasegawa, J.; Ishida, M.; Nakajima, T.; Honda, Y.; Kitao, O.; Nakai, H.; Vreven, T.; Montgomery, J. A., Jr.; Peralta, J. E.; Ogliaro, F.; Bearpark, M.; Heyd, J. J.; Brothers, E.; Kudin, K. N.; Staroverov, V. N.; Kobayashi, R.; Normand, J.; Raghavachari, K.; Rendell, A.; Burant, J. C.; Iyengar, S. S.; Tomasi, J.; Cossi, M.; Rega, N.; Millam, J. M.; Klene, M.; Knox, J. E.; Cross, J. B.; Bakken, V.; Adamo, C.; Jaramillo, J.; Gomperts, R.; Stratmann, R. E.; Yazyev, O.; Austin, A. J.; Cammi, R.; Pomelli, C.; Ochterski, J. W.; Martin, R. L.; Morokuma, K.; Zakrzewski, V. G.; Voth, G. A.; Salvador, P.; Dannenberg, J. J.; Dapprich, S.; Daniels, A. D.; Farkas, O.; Foresman, J. B.; Ortiz, J. V.; Cioslowski, J.; Fox, D. J. *Gaussian 09*, revision D.01; Gaussian, Inc.: Wallingford, CT, 2009.

(39) Schuchardt, K. L.; Didier, B. T.; Elsethagen, T.; Sun, L.; Gurumoorthi, V.; Chase, J.; Li, J.; Windus, T. L. *J. Chem. Inf. Model.* **2007**, *47*, 1045–1052.

(40) Feller, D. *J. Comput. Chem.* **1996**, *17*, 1571–1586.

(41) Hintermair, U.; Sheehan, S. W.; Parent, A. R.; Ess, D. H.; Richens, D. T.; Vaccaro, P. H.; Brudvig, G. W.; Crabtree, R. H. *J. Am. Chem. Soc.* **2013**, *135*, 10837–10851.

(42) Brereton, K. R.; Pitman, C. L.; Cundari, T. R.; Miller, A. J. M. *Inorg. Chem.* **2016**, *55*, 12042–12051.

DOI: 10.1021/acs.organomet.7b00175
Organometallics XXXX, XXX, XXX–XXX